*Coastal Dynamics 2017*

*Paper No. 129*

# WAVE AND CURRENT RIPPLE FORMATION AND MIGRATION DURING STORMS

Meagan E. Wengrove[1], Diane L. Foster[2], Matthieu A. de Schipper[3], and Thomas C. Lippmann[4]

**Abstract**

Field observations of bedform response to combined wave-current flows were obtained within the surf zone along the Delfland coast, The Netherlands, as part of the MEGAPEX Field Experiment in the fall of 2014. Fine scale seafloor topography was observed with a rotating pencil beam sonar along with co-located observations of waves and currents. New methods for sonar processing were implemented to find fluid-sediment boundaries, quantify bedform geometry, and estimate bedform migration rates. Observed bedform geometries with wavelengths ranging from 0.14 to 2.5 m and migration rates between 0 and 3 cm/min are strongly influenced by variations in the flow field due to the spring-neap tidal cycle as well as forcing from several storm events. Results suggest that the combined effects of storm waves and mean currents most strongly influence small scale morphodynamic behaviors.

**Key words:** bedforms, combined flows, currents, sediment transport, morphodynamics, field experiment

## 1. Introduction

In coastal environments small scale bed roughness (e.g. sand ripples) can have a significant influence on local hydrodynamics (Traykovski et al., 1999). In the nearshore, waves, tidal currents, river currents, storm surge, and alongshore currents can each contribute significantly to local morphodynamics. In particular, a nonlinear combination of waves and currents can strongly influence bedform geometries and sediment transport (Lacy et al., 2007). Many field and laboratory observations of bedform evolution have been made under wave dominated conditions (see Soulsby et al., 2005); however, far fewer have been made under combined wave-current flows (e.g. Li and Amos, 1998; Gallagher et al., 1998; Lacy et al., 2007; Larsen et al., 2015). Significant differences exist between current generated bedforms and those generated by waves (Fredsøe and Deigaard, 1992), and so parameterizing roughness in combined flows using results from only-wave or only-current conditions may lead to misrepresentation of sediment transport flux estimates in morphologic modeling. In order to better predict the effects of bedforms on larger scale sediment transport patterns, it is important to improve understanding hydrodynamic forcing drives the evolution of small scale coastal morphology, and the influence that combined flows have upon these changes.

Surf zone observations of wave and current induced bedform formation and migration during spring-neap tidal variations and the passing of several storms were made on the Delfland coast of The Netherlands. Data were collected at the Sand Engine as a part of the MEGA-Perturbation EXperiment (MEGAPEX) in the fall of 2014. Since the installment of the 20 million cubic meter sand mega-nourishment in 2011, nearshore morphology has dramatically changed shape; in 2011 the Sand Engine extended 2 km in the alongshore and 1 km into the North Sea, and by 2014 it stretched to 4.5 km alongshore and contracted to 700 m seaward (Stive, et al. 2013; Radermacher, et al. 2017).

Our research focus is on fine scale spatial and temporal resolution of seafloor morphology that respond to the combined influence of storm waves and strong currents in the nearshore, and forms one of few observational data sets of bedforms under combined wave-current flows.

[1] Ocean Engineering, University of New Hampshire (UNH). med36@wildcats.unh.edu
[2] Department of Mechanical Engineering and Ocean Engineering, UNH. diane.foster@unh.edu
[3] Hydraulic Engineering Department, CiTG, Technical University of Delft. m.a.deschipper@tudelft.nl
[4] Center for Coastal and Ocean Mapping and Department of Earth Sciences, UNH. lippmann@ccom.unh.edu

## 2. Methods

### 2.1. *Instrumentation*

Local small scale morphology and hydrodynamics were observed just seaward of the low tide shoreline at the tip of the Sand Engine (Figure 1). Seafloor topography was obtained with a stationary sweeping and incrementallyrotating 1 MHz Imagenex 881a pencil beam sonar with a 3 m diameter footprint, sampled every 20 minutes with a 1.4° sweep step and a 2.4° rotation step from 26 Sept. to 23 Oct. 2014 (day of year 269-296). The vertical profile of horizontal currents measured using a downward looking high resolution acoustic Doppler current profiler (ADCP) positioned ~0.4 m above the bottom boundary and sampled at 4 Hz in 20 minute bursts every hour. The mean low water depth was -0.3 m NAP (Normaal Amsterdams Peil) and the median sediment grain size was 350 μm. Generally, the tidal range was approximately 1.5 m. These observations were collected just seaward of the shore break.

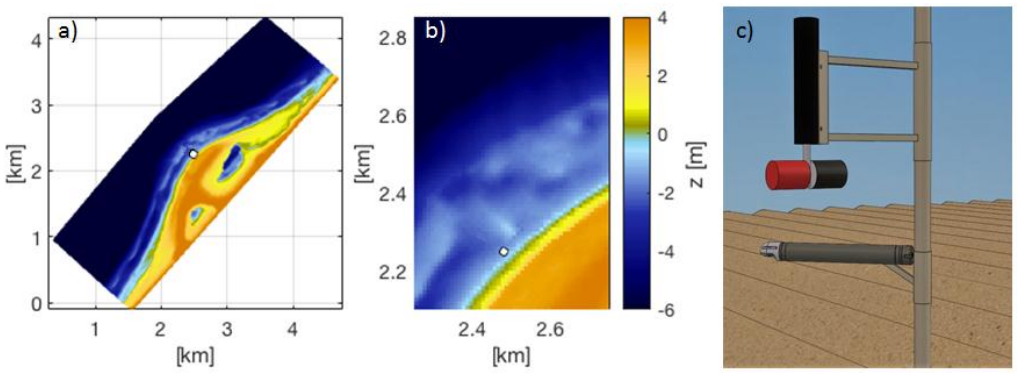


Figure 1. Sampling location and instrument set up. a) Sand Engine mega-nourishment, North is toward the positive y-axis, East is toward the positive x-axis. b) Close-up showing sampling location marked by white circle. c) Schematic showing instrument setup; upper instrument is an Imagenex pencil beam sonar (located 1 m from the boundary); lower instrument is a downward looking high resolution ADCP (located 0.4 m from the boundary).

### 2.2. *Morphologic Statistics*

Statics of bedform wavelength ($\lambda$), height ($\eta$), direction ($\phi$), migration rate ($V_{mig}$), and migration direction ($\phi_{mig}$) are determined through analysis of sonar return data. These statistics can be determined using processed bathymetries found through analysis of the sonar intensity data for every sonar sweep (e.g. Figure 2).

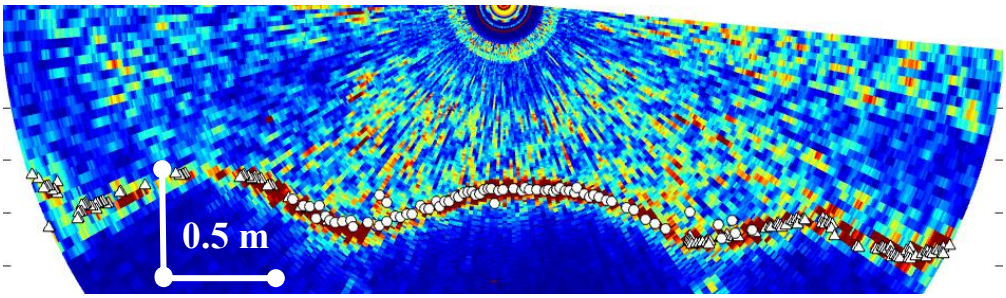


Figure 2. Ripple profile at peak of storm showing wavelength of 2 m and height of 25 cm (Julian day 295.05 for reference to time series in Figure 4). Image color scale is intensity of acoustic return, where reds are high intensity and blues are low intensity. Bottom return is indicated by the dark red line signal. The sonar head is located at the top center of the image. The white circles are the result of the WMS bottom finding method and the white triangles are the result of the BDI bottom finding method. Scale bars are shown in lower left hand corner.

2.2.1. *Bottom Finding*

Bottom position within each sonar dataset was found by identifying the high intensity return region for each sonar ping using two methods. The first is a weighted mean sum (WMS) method, which works well for return data with high grazing angles (data within ~30° of the sonar nadar). The second is a bearing direction indicator (BDI) method, which works well for intensity returns at low grazing angles. WMS is applied to each sonar ping return time series and BDI is applied considering every sonar ping return time series in an entire sonar sweep (see Figure 2). The sweep is composed of many sonar pings, each originating from the sonar head (Figure 2). This assumes that the acoustic return for each ping within a sweep is the same with respect to the relative time of the return pulse. Using estimates of sound speed and ping angle, return time, $t$, can be transformed into a distance from the sonar head, so within each sweep the coordinate system is ($s$, $z$), where $s$ is the horizontal distance away from the sonar head, and $z$ is the vertical distance away from the sonar head. A sonar ping return time series for any given direction is henceforth referred to as an individual beam.

The WMS method is defined by a summation over time of return along an individual beam,

$$WMS = \frac{\sum_{t=1}^{T} n_t^{\beta} n_t}{\sum_{t=1}^{T} n_t^{\beta}}, \tag{1}$$

where, $n_t$ is the acoustic return time along any beam, $n$, from the sonar head to the extent of the collection (somewhere below the boundary return), and $\beta$ is a weighting factor, set to 10 (SeaBeam, 2000). The location of the highest WMS for each beam is the ($s$, $z$) location of the bed.

The BDI method assumes that every sweep of the pencil beam sonar is analogous to one pulse from a multi-beam sonar. At low grazing angles, multiple beams in a sweep for a given time, $t$, will capture a return from the same piece of boundary, especially if there are bedforms present. By combining the return information from all beams gives a better estimation of the location of the bed. In essence, the BDI method takes into account the intensity peaks of all beams in a given sweep for some return time. Each peak with intensity greater than a given noise threshold are fit with a 3-5 point parabola. Within a given sweep, at locations where the return signal is interacting with the boundary at a low grazing angle, there will be two parabolic fits to the signal return, one for the $+s$ direction from the sonar head and one for the $-s$ direction. In the ideal case the center peak in both directions will have the strongest intensity return. The peak of the fitted parabola in Cartesian coordinates is the ($s$, $z$) location of the bed (SeaBeam, 2000).

After all ($s$, $z$) bed locations are determined using both WMS and BDI, the respective sweeps are rotated in a horizontal plane around the sonar head to determine the relative ($x$, $y$, $z$) position rendering a local bathymetric map for each sonar run.

2.2.2. *Estimating Bedform Geometry and Migration Rates*

From the 2D local bathymetry maps, the dominant ripple wavelengths, heights, and orientations are determined with 2D spatial spectral analysis (Maier and Hay, 2009; Becker et al., 2007). The 2D spatial spectra have axes of wavenumber, $k_x$ and $k_y$ (1/m), and energy density, $S$ ($m^4$). The location of the dominant peaks in the spectra indicate the associated bedform wave number, where bedform wavelength, orientation, and height are defined, respectively.

$$\lambda = 2\pi/(k_x^2 + k_y^2)^{0.5}, \tag{2}$$

$$\phi_r = \mathrm{atan}(k_y/k_x), \tag{3}$$

$$\eta = 4\sqrt{\int\int \eta(k)^2 dk_x dk_y}. \tag{4}$$

The calculation of bedform height, $\eta$, is analogous to a significant ocean wave height calculation from temporal spectral analysis (Traykovski, 2007; Penko, et al., 2016). Figure 3 shows three example bathymetries and their corresponding 2D spectra.

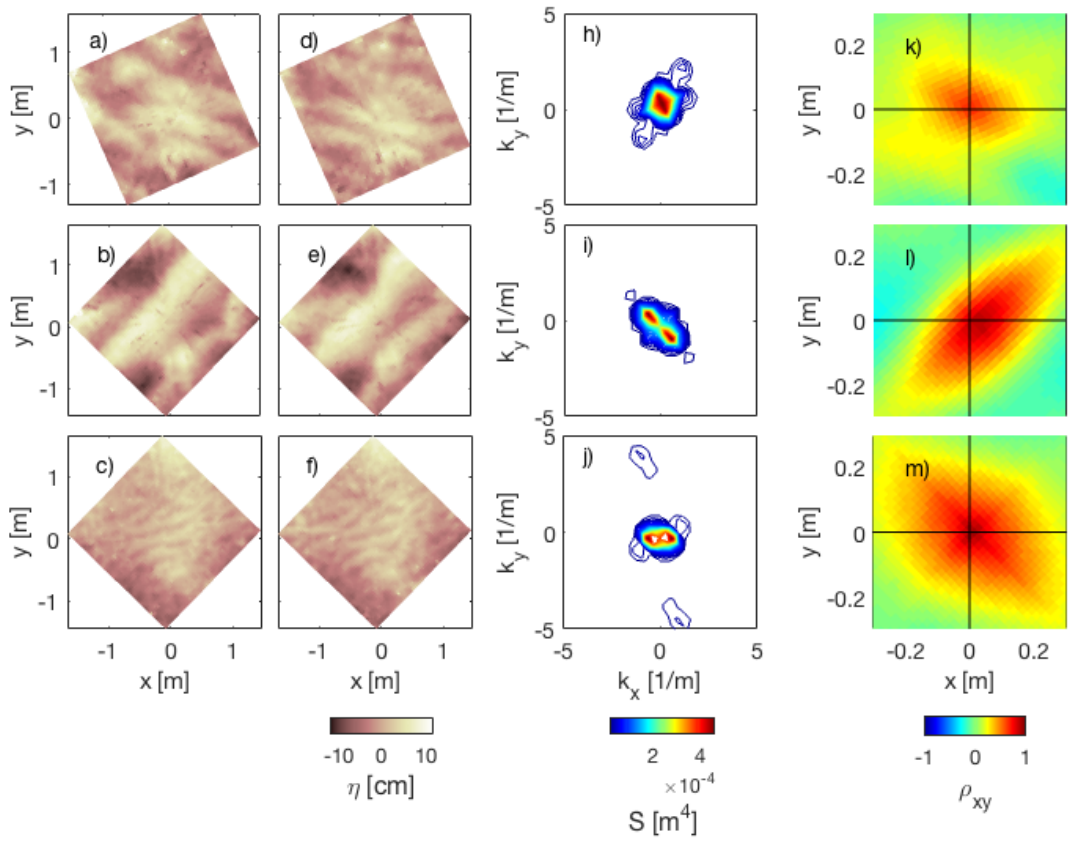


Figure 3. Bathymetry maps (a-f) and 2D spectra of a-c (h-j) and 2D cross correlations between a-d, b-e, and c-f (k-m). Orientation of image is –y directed onshore, +x directed towards the NE, -x directed toward the SW as seen in Figure 1. (a-f) Local bathymetry maps found using the WMS and BDI methods. (h-j) 2D spectra of bathymetries a-c, respectively. Orientation of lobes shows orientation of bedforms, and position of lobe corresponds to bedform wavenumber. (k-m) 2D cross correlation between bathymetric pairs. The location of peak correlation corresponds to the magnitude and direction of bedform migration between bathymetric pairs. Ex: Panel b) has a wavelength of 1.1 m, orientation of 45° from shore normal to the NE; migration distance in a 20 minute period between image pairs is 7 cm, which corresponds to a migration rate of 0.35 cm/min; migration direction is 80° from shore normal to the NE.

To find migration rates and migration directions a 2D cross correlation was used. The 2D cross correlation, $\rho_{xy}$, is defined as

$$\rho_{xy} = \frac{(x_t - \mu_x)(y_t - \mu_y)}{\sigma_x \sigma_y}, \tag{5}$$

where, $x$ and $y$ indicate the subsequent bathymetries in time that are being compared spatially, $\mu$ is the mean, and $\sigma$ is the standard deviation (Bendat and Piersol, 2010). From the maxima ($x_m$, $y_m$) in the 2D cross correlation, the migration rate and migration direction can be found, respectively, by

$$V_{mig} = \frac{\sqrt{x_m^2 + y_m^2}}{t_s}, \tag{6}$$

$$\phi_{mig} = \mathrm{atan}(y_m / x_m), \tag{7}$$

respectively, where $t_s$ is the time between the subsequent bathymetry pair. Figure 3 shows three example bathymetry pairs and their corresponding 2D cross correlation.

### 2.3. *Hydrodynamic Statistics*

Hydrodynamic statistics were calculated using measured velocity components from the ADCP. The current velocity, $U$, and direction, $\phi_c$, were found, respectively, by

$$U = \sqrt{\overline{u}^2 + \overline{v}^2}, \tag{8}$$

$$\phi_c = \mathrm{atan}(\overline{v}/\overline{u}), \tag{9}$$

where $u$ and $v$ are the horizontal components of velocity and the overbar represents a 10 minute mean. By removing the mean current,

$$u_w = \sqrt{u^2 + v^2} - U \tag{10}$$

the orbital velocity, $u_o$, is calculated using the root mean square velocity as

$$u_o = \sqrt{2}\sqrt{\overline{|u_w^2|}} \tag{11}$$

and the direction of the waves, $\phi_w$, is defined with

$$\phi_w = \mathrm{atan}((v - \overline{v})/(u - \overline{u})). \tag{12}$$

## 3. Results and Discussion

### *3.1 Hydrodynamics*

Bedform geometry and orientation is a result of the hydrodynamic forcing imposed upon the boundary. Time series of bedform wavelength, orientation, migration rate, and migration direction are shown in Figure 4d and 4e, along with time series of water depths (4a), mean current magnitude (4b), and rms orbital

velocities (4c). The variability in hydrodynamic forcing drives the bedform geometry and migration patterns. The color scale represents flow direction, bedform orientation, or bedform migration direction. The magnitude and direction of the current indicate that the mean current is highly dominated by tides. The predominant tidal orientation on the Delfland coast is shore parallel, with flood tides directed toward the NE and ebb tides toward the SW (see Figure 1 for reference). The magnitude of the current during flood tide is generally stronger than during ebb tide; however, with additional storm forcing the wave-driven flow exceeds the tidal flow in the inner surf zone. The time series goes through 2 spring-neap cycles and has 4 storm events (indicated in Figure 5). Spring flood tidal currents are stronger than those during neap.

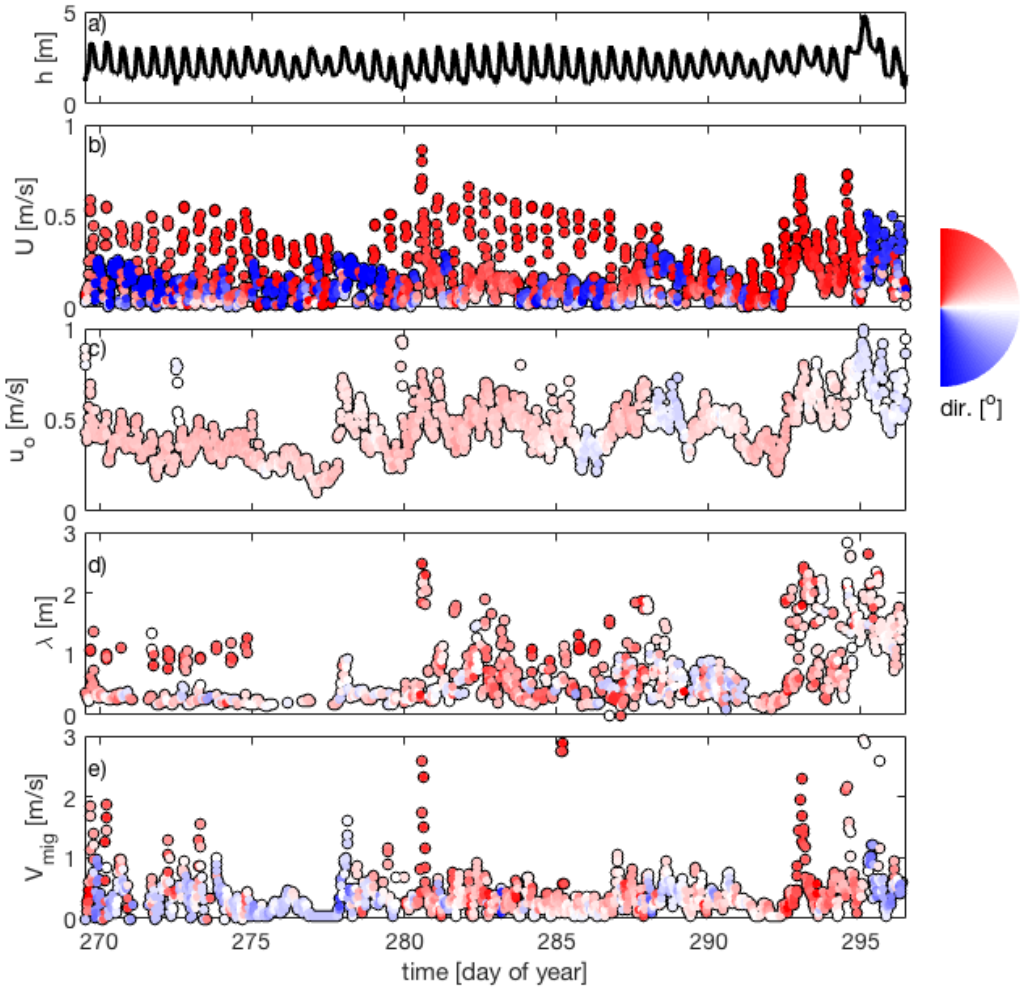


Figure 4. Time series of hydrodynamic and bedform statistics colored by flow direction or bedform orientation as indicated by the color wheel (white is directed onshore, dark red and blue are alongshore, with red flowing or oriented toward the NE and blue toward the SW as seen in Figure 1). a) depth. b) current magnitude. c) wave orbital velocity. d) bedform wavelength. e) bedform migration rate.

At the Sand Engine, wave forcing is driven by frequent offshore storms lasting typically 1-3 days. The magnitude of the wave orbital velocity at the sampling location within the inner surf zone (Figure 4c) increases with the onset of storms but is tidally modulated due to wave breaking on the offshore sandbar at lower stands of the tide. In general, waves came from the NW during the experiment and strike the coast at an angle driving a longshore current to the SE.

### *3.2 Bedform Geometry and Mobility in Response to Waves and Currents*

Bedform wavelengths (Figure 4d) and migration rates (Figure 4e) are influenced by both mean currents and waves. During spring tide (day of year 270-275) bedform wavelengths and migration rates are strongly influenced by large tidal currents, increasing and decreasing as a function of current magnitude. At day of year 278, 281, 283, and 293, the bedform wavelengths and migration rates increase during the passing of a storm. Bedform migration direction is qualitatively influenced by the direction of the current. Bedform migration direction is influenced by both wave direction and current direction with a bias toward the direction of the currents. Bedform orientation shows similar patterns, but is not as strongly influenced by current direction. The largest and most mobile bedforms occur when both the waves and currents are strongly contributing to the hydrodynamic forcing (as seen between day of year 293 and 296).

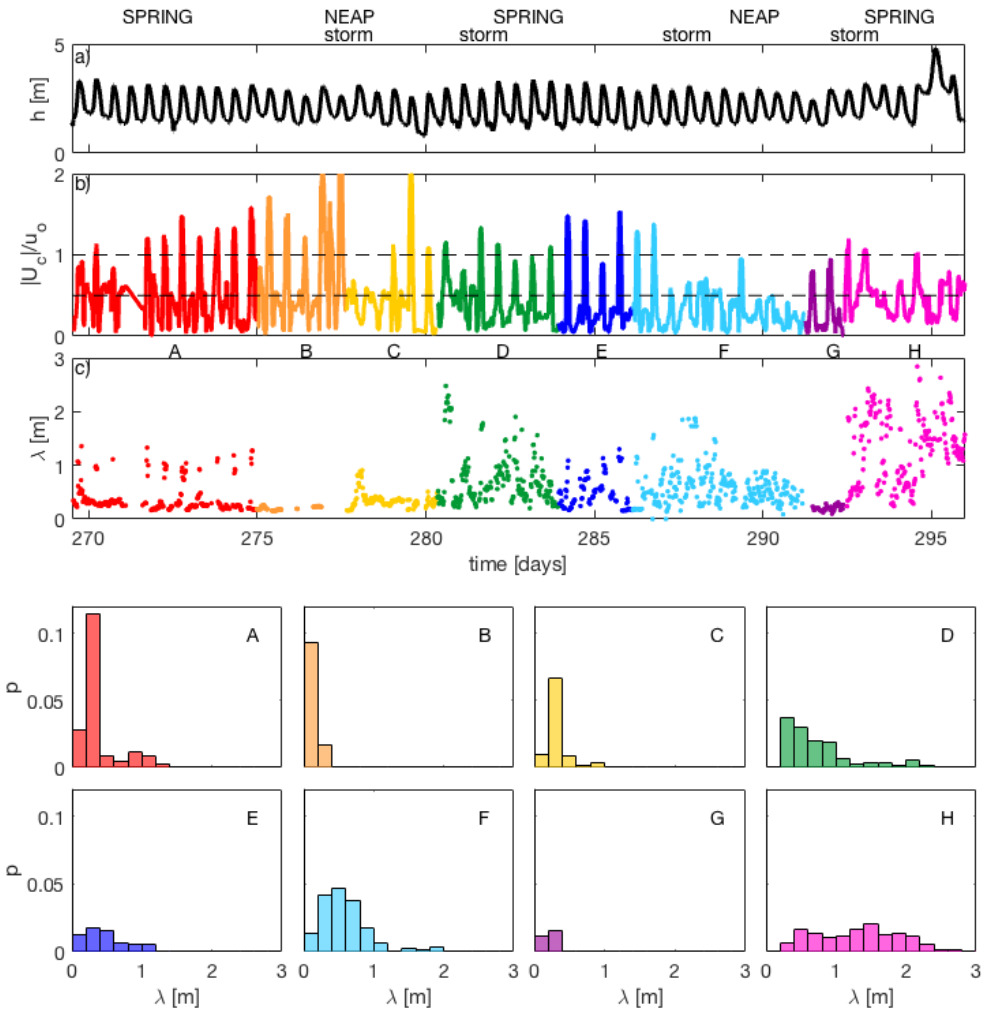


Figure 5. Time series of hydrodynamic forcing ratio and corresponding histograms of bedform wavelength for each forcing segment. Each histogram accounts for only those bedforms occurring within that highlighted segment; however distribution probability is relative to all observations, and hence the probability of occurrence, p, for any individual wavelength within each distribution is small. Spring tide, neap tide and periods with additional storm forcing are labeled above the top panel. a) Time series of depth. b) Time series of ratio of current velocity and wave orbital velocity colored in segments by periods of spring tide and neap tide with or without added storm forcing. Dashed lines indicate thresholds for wave dominant, combined wave-current dominant, and current dominant forcing as described in the text. c) Time series of bedform wavelength colored in same way as panel b. A-H are corresponding histograms of bedform wavelength for each colored and labeled segment as seen in panel b and c.

To examine the relationship between bedform geometry shifts and variability in hydrodynamics, the time series is segmented based upon forcing conditions, and a histogram of bedform wavelength is computed for each segment (Figure 5). Figure 5b shows a ratio of current magnitude to wave orbital velocity, analogous to Li and Amos (1998), where bedforms are thought to be wave formed when $U/u_o \leq 0.5$, combined wave current formed when $0.5<U/u_o \leq 1$ or current formed when $U/u_o > 1$. Segments A and E show spring tide without storm forcing, B and G show neap tide without storm forcing, C and F show neap tide with storm forcing, and D and H show spring tide with storm forcing.

When comparing periods of spring tide to neap tide without storm forcing, spring tide histograms A and E show an occurrence of larger wavelength bedforms (0.8 m or greater) that are not evident during neap tide without storms (B and G). When viewing histogram A in light of Figure 5b and 5c, it is evident that these larger wavelength bedforms were formed with the onset of strong currents. During neap tide the flood tide current is much weaker than during spring tide and does not likely generate these large wavelength bedforms. Even though segment B shows data with $U/u_o > 1$, which would indicate current induced bedforms, the magnitude of the current and orbital velocities during this period are low, suggesting that in this case current dominance erodes existing bedforms rather than forms new bedforms. Without storms, bedforms formed during neap tide and in-between periods of strong current during spring tide are wave induced ($U/u_o \leq 0.5$).

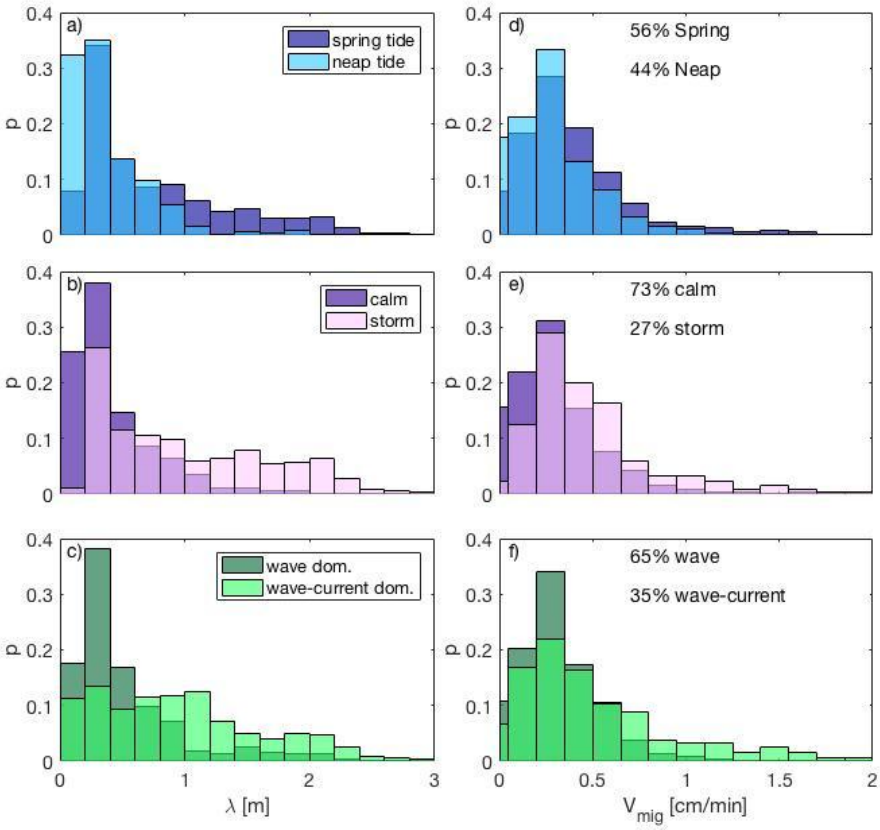


Figure 6. Histograms of bedform wavelength and migration rates based upon legend data segmentations. Within each panel, each histogram distribution is relative to itself and not to the entire dataset, meaning in panels a) and d) the distribution of bedform wavelength and migration rate is accounting for instances occurring within only spring tide or only neap tide. The percent of the dataset that falls within spring tide or neap tide is labeled in the upper right hand corner of d) for both panels. b) and e) Histograms of bedform wavelength and migration rate, respectively, segmented by periods of calm and storm. The percent of the dataset that falls within calm and storm periods are labeled in the upper right hand corner of e) for both panels. c) and f) Histograms of bedform wavelength and migration rate, respectively, segmented by periods of wave dominated flow and combined flow. The percent of the dataset that falls within wave dominated and combined flow conditions is labeled in the upper right hand corner of f) for both panels.

When storms do occur during neap tidal periods (C and F), there are a few instances of larger wavelength bedforms; however during these periods $U/u_o$ is generally $\leq 0.5$, suggesting that these wave formed bedforms as well. The wavelength of these bedforms is at times longer due to the larger storm waves. The largest wavelength and most dynamic bedforms occur during spring tide with the onset of a storm (D and H). The hydrodynamic forcing is greatest during the D and H segments (Figure 4b and 4c), and these bedforms were at times wave induced, current induced, or combined wave-current induced, with the largest bedforms being formed during periods of combined wave-current forcing (Figure 5b).

Observations of bedform geometry and mobility at the Sand Engine are observed to be variable based on the phase of the tide as well as the presence of a storm. Histograms of bedform wavelength and migration rates are segmented into observations based upon spring tide and neap tide (Figure 6a and 6d), calm and storm conditions (Figure 6b and 6e), and wave dominant ($U/u_o \leq 0.5$) and current or combined flow dominant ($U/u_o > 0.5$) (Figure 6c and 6f). These histograms are relative to only the data in the respective segment, rather than the entire set of observations as was the case for the histograms in Figure 5. The percentage of data falling into each segment is marked in the upper right hand corner of the right hand panels in Figure 6. These 12 histograms summarize factors driving bedform transformation and mobility during the deployment.

As bedforms get larger they can have a progressively greater influence on the local hydrodynamics. With the addition of increased bedform migration rates that move more sediment, the effect on coastal change could be more important. This suggests that the occurrence of larger wavelength bedforms ($\lambda \geq 0.8$ m) with increased migration rates ($V_{mig} \geq 1$ cm/min) may be disproportionally important to the net transport.

Although there were many observed occurrences of smaller wavelength bedforms ($\lambda < 0.8$ m) during all tides, there were slightly (10%) more, larger wavelength bedforms ($\lambda \geq 0.8$ m) during spring tides (Figure 6a). A similar variation is observed in the migration rate, with 5% increased occurrence of larger migration rates during spring tide compared to neap tide.

During the experiment storm conditions were present for 27% of the dataset. Under storm forcing, there is a 20% increase in occurrence of larger wavelength bedforms and an 8% increase in occurrence of higher bedform migration rates (Figure 6b and 6e) compared to calm conditions. Although during spring and neap tidal periods two storms of similar magnitude occurred, the spring tide bedforms had a higher frequency of occurrence of larger wavelength bedforms than neap tide (Figure 6a), a result that can be attributed to strong tidal currents of spring tide (as seen in Figure 4) in conjunction with additional storm forcing. Spring tides with the addition of storm waves had a 42% increase in occurrence of larger wavelength bedforms and a 5% increase of higher migration rates when compared to the rest of the dataset (Figure 5, periods D and H).

Histograms shown in Figure 6c and 6f show that combined flows are responsible for a 14% increase in occurrence of larger wavelength bedforms and a 13% increase in occurrence of higher migration rates when compared to the distributions of wave dominant flows only.

The influence of combined flows ($0.5 < U/u_o \leq 1$) on bedform wavelength and migration rates is shown in Figure 7. Bedforms with wavelengths greater than 0.8 m can occur during wave dominant, combined wave-current dominant, and current dominant forcing conditions with variable migration rates (from no migration to high migration). However, the largest observed migration rates occurred during periods of combined flows and slightly current dominated flows (it should be noted that there are a few occurrences of large migration rates in wave dominant conditions, possibly due to wave asymmetries when waves get large). Within combined flow conditions, as migration rates increase, bedform wavelengths are also generally larger. These large and rapidly migrating bedforms are likely to be transporting the most sand per unit time and are linked to flow conditions characterized by strong tidal currents coincident with storm waves (Figure 5).

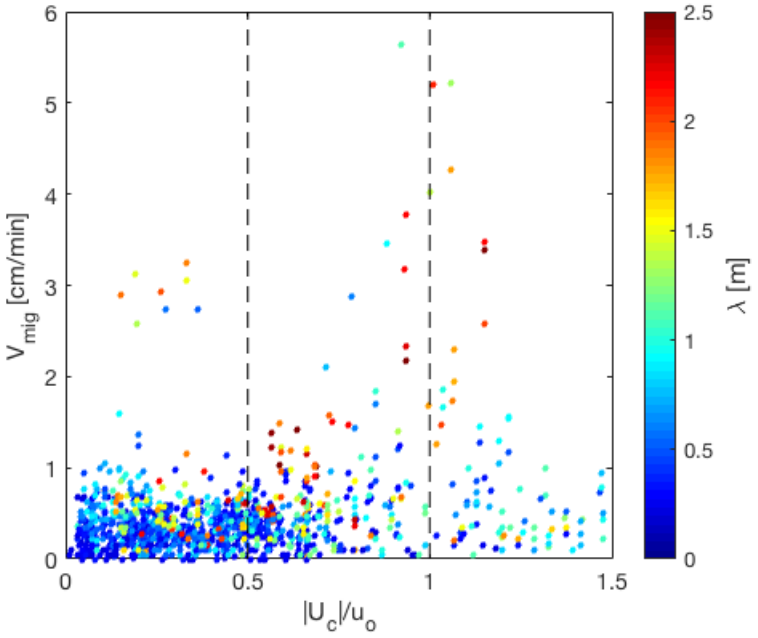


Figure 7. Scatter plot of the ratio of current velocity to orbital velocity plotted against bedform migration rate and colored by bedform wavelength. Dashed lines indicate cutoffs for defined wave, wave-current, and current dominant conditions.

## 4. Conclusion

Observations of local hydrodynamics and morphology indicate that both wave and mean current forcing contribute to the transformation and migration of nearshore bedforms during both calm and storm conditions. At the Sand Engine, bedform dynamics are strongly tidally regulated and greatly influenced by additional forcing from storms.

With the presence of a storm and in the absence of strong spring tidal currents, bedforms are generally wave dominated. Wave dominated bedforms can become large depending upon the size of the waves. Additionally, bedforms are shown to become purely current driven during spring flood tides in the absence of an imposed storm. Within these field observations, the largest and fastest moving bedforms occurred during combined flows during spring tides and storm waves, suggesting that combined forcing events may have the greatest influence on morphodynamics.

Overall, results show that combined flows can substantially contribute to changes in nearshore morphology, more than with wave or current forcing alone. Often, sediment transport models account for transport due to waves or due to currents, but not the combined effects of wave-current forcing. This research suggests that combined flow effects are important to bedform geometries and migration, and should be considered within sediment transport models. Examination of the combined flow effects upon bedform formation and influence upon sediment transport flux as well as its contribution to local coastal change is the subject of ongoing research.

## Acknowledgements

Funding for our field efforts during MEGAPEX was provided by the PADI Foundation, ERC – advanced grant 291206-NEMO, and UNH. MEW is supported by a U.S. DOD NDSEG fellowship. MAdS is financed by NWO Domain Applied and Engineering Sciences under project code 15058. TCL was supported by the Office of Naval Research.

## References

Bendat, J. S. and A. G. Piersol, 2010. *Random Data*. John Wiley and Sons.

Becker, J. M., Y. L. Firing, J. Aucan, R. Holman, M. Merrifield, and G. Pawlak, 2007. Video-based observations of nearshore sand ripples and ripple migration. *Journal of Geophysical Research*, 112.

Fredsøe, J., and R. Deigaard, 1992. *Mechanics of coastal sediment transport*. World Scientific.

Gallagher, E. L., S. Elgar, and E. B. Thornton, 1998. Megaripple migration in a natural surf zone. *Letters to Nature*, 394.

Lacy, J. R., D. M. Rubin, H. Ikeda, K. Mokudai, and D. M. Hanes, 2007. Bed forms created by simulated waves and currents in a large flume. *Journal of Geophysical Research*, 112.

Larsen, S. M., B. Greenwood, and R. Aagaard, 2015. Observations of megaripples in the surf zone. *Marine Geology*, 364.

Li, M. Z., and C. L. Amos, 1998. Predicting ripple geometry and bed roughness under combined waves and currents in a continental shelf environment. *Continental Shelf Research*, 18, 941–970.

Maier, I., and A. E. Hay, 2009. Occurrence and orientation of an orbital ripples in near- shore sands. *Journal of Geophysical Research*, 114.

Penko, A., J. Calantoni, and B. T. Hefner, 2016. Modeling and observations of sand ripple formation and evolution during trex13, *Journal of Oceanic Engineering*.

Radermacher, M., M. A. de Schipper, C. Swinkles, J. H. MacMahan, A. J.H.M. Reniers, 2017. Tidal flow separation at protruding beach nourisments, *Journal of Geophysical Research:Oceans*.

SeaBeam, 2000. Multibeam sonar theory of operation, Tech. rep., L3 *Communications of SeaBeam Instruments*.

Soulsby, R. L., R. J. S. Whitehouse, and K. V. Marten, 2005. Prediction ripple properties in shelf seas. *HR Wallingford Report*, TR 150.

Stive, M. J. F., M. A. de Schipper, A. P. Luijendijk, S. G. J. Aarninkhof, C. van GelderMaas, J. S. M. van Thiel de Vries, S. de Vries, M. Henriquez, S. Marx, and R. Ranasinghe, 2013. A new alternative to saving our beaches from sea-level rise: The sand engine. *Coastal Engineering*, 29(5).

Traykovski, P., A. E. Hay, J. D. Irish, and J. F. Lynch, 1999. Geometry, migration, and evolution of wave orbital ripples at leo-15. *Journal of Geophysical Research*, 104(C1), 1505–1524.

Traykovski, P, 2007. Observations of wave orbital scale ripples and a nonequilibrium time-dependent model. *Journal of Geophysical Research*, 112(C06026)